

Supporting Information

Thermally Activated Carbon-Nitrogen Vacancies in Double-Shelled NiFe Prussian Blue Analogue Nanocages for Enhanced Electrocatalytic Oxygen Evolution

**Miaomiao Jiang, Xiaoming Fan,* Shuai Cao, Zihan Wang, Zeheng Yang and Weixin
Zhang***

School of Chemistry and Chemical Engineering

Hefei University of Technology

Hefei, Anhui 230009, P. R. China

*Correspondence: xmfan@hfut.edu.cn (X. Fan), wxzhang@hfut.edu.cn (W. Zhang)

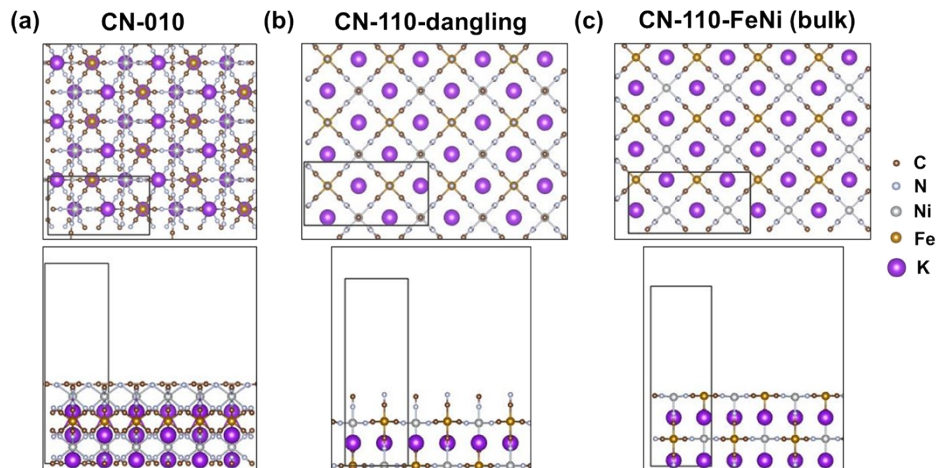


Fig. S1. Initial structures for different crystal surfaces (a) CN-110, (b) CN-010-dangling and (c) CN-010-FeNi, and the bulk CN-bulk. (CN-010-FeNi and CN-bulk have the same initial structure)

The departure of surface CN are discussed by three kinds of models, one from (010) surface (marked as CN-010), and the other two from (110) surface. In particular, for (110) surface, the two models are the CN connected with Ni with a dangling bond (marked by CN-110-dangling) and the CN bridges Ni and Fe (CN-110-FeNi). Their initial structures, namely, the structures before CN departure begins are shown in Fig. S1.

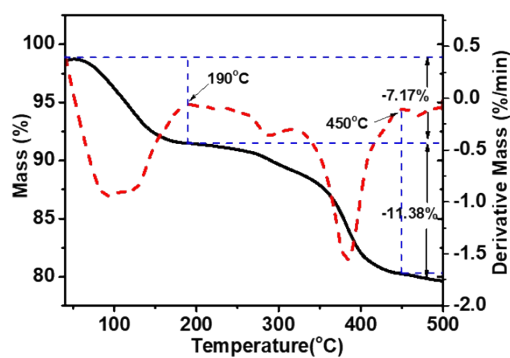


Fig. S2. TG-DTA characterization of as-prepared double-shelled PBAs-NG.

Thermogravimetric technique was used to monitor the thermal stability of NiFe PBAs in nitrogen atmosphere (Fig. S2). At first step from room temperature to 190 °C, NiFe PBAs undergo dehydration to the intermediate state with preserving physical characters. With further temperature increase to 450 °C, the weight loss related with the ongoing decomposition process which gives a new phase attributed to the newly generated composite.

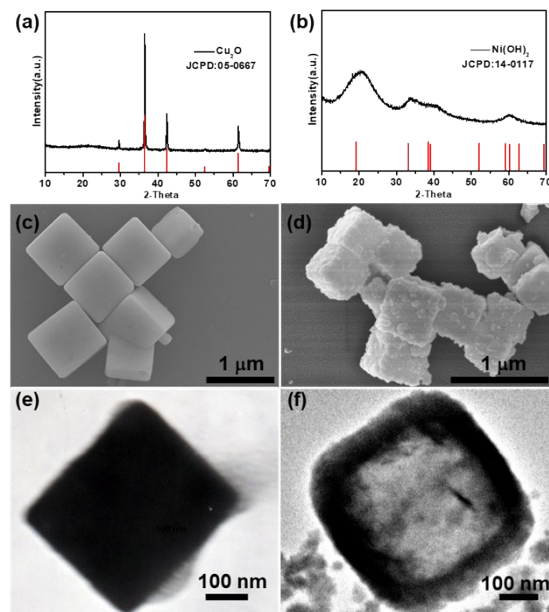


Fig. S3. (a, b) XRD pattern of Cu_2O and $\text{Ni}(\text{OH})_2$. SEM images and TEM images of (c, e) Cu_2O and (d, f) $\text{Ni}(\text{OH})_2$.

The as-synthesized Cu_2O nanocubes can be clearly indexed to the cubic phase (JCPDS No. 05-0667) (Fig. S3a), and show smooth surface and uniform size with a side length of ~ 500 nm evidenced by the scanning electron microscopy (SEM) images (Fig. S3c). The solid Cu_2O nanocubes (Fig. S3e) were then completely transformed into $\text{Ni}(\text{OH})_2$ nanocages through Pearson's HSAB principle, which has been described in the experimental section. X-ray powder diffraction (XRD) characterization confirms the successful transformation from Cu_2O nanocubes to $\text{Ni}(\text{OH})_2$ nanocages with a poor crystallinity (Fig. S3b). Typical SEM and TEM (Fig. S3d and S3f) images exhibit that the as-prepared hollow $\text{Ni}(\text{OH})_2$ products are exclusively high-quality single-shelled nanocages with rough surface, which inherit the sizes and geometric shapes of the Cu_2O nanocubes templates well, with a uniform side length of ~ 450 nm and wall thickness of 80-100 nm.

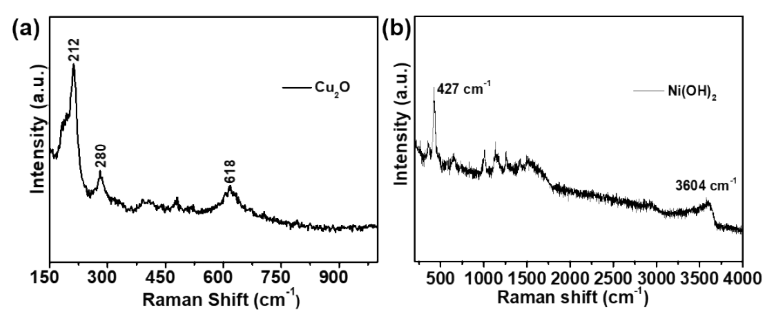


Fig. S4. Raman spectra of (a) the Cu₂O nanocubes and (b) Ni(OH)₂ nanocages.

Raman spectroscopy analysis (Fig. S4a) further confirm the crystalline phase of Cu₂O with well-defined second-order overtone at $\sim 212\text{ cm}^{-1}$.¹ By comparison, the Ni(OH)₂ nanocages show the A_{1g} lattice mode existing at 446 cm^{-1} and the A_{1g} O–H stretch at 3604 cm^{-1} (Fig. S4b).^{2,3}

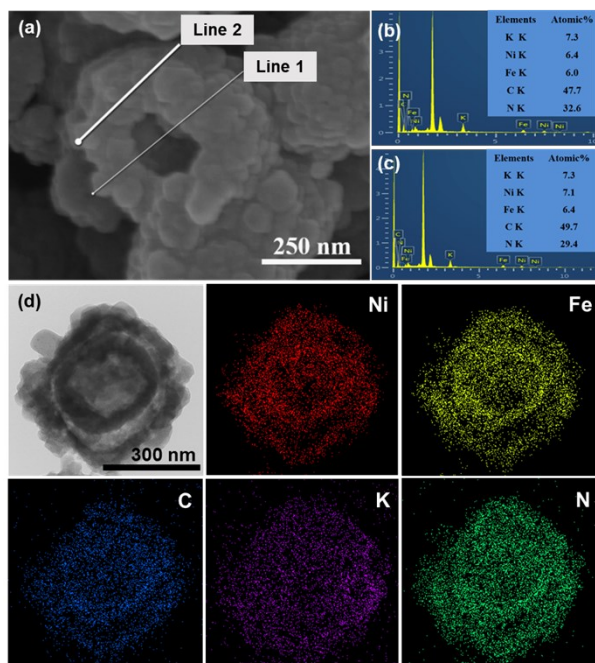


Fig. S5. (a) SEM image, and (b, c) EDS line scanning in the SEM image of PBAs-3. (d) EDS mapping of PBAs-3.

Fig. S5 proves that the as-prepared NiFe PBAs obtained by ion-exchange reaction at room temperature for 24 h has typical double-shelled hollow hierarchical architecture and homogenous composition, in which Fe/Ni atomic ratios obtained from EDS line scanning spectrum are close to the stoichiometric ratio of 1:1 that consistent with its composition $(K_2NiFe(CN)_6)$.

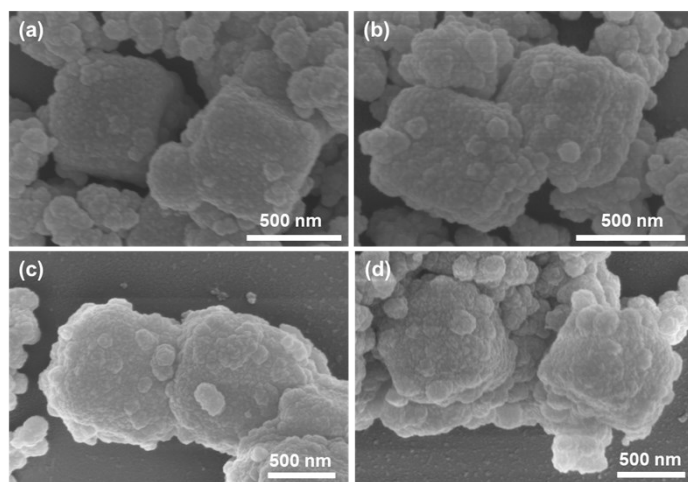


Fig. S6. SEM images of (a) PBAs-1, (b) PBAs-2, (c) PBAs-3 and (d) PBAs-4.

With the extension of the ion exchange time, we can observe the distinct $\text{Ni}(\text{OH})_2$ nanocages were transformed to rough hierarchical NiFe PBAs nanocages.

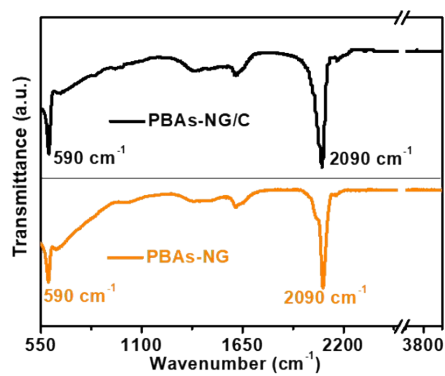


Fig. S7. FT-IR spectra of PBAs-NG and PBAs-NG/C.

The as-prepared PBAs-NG/C reflected in FT-IR spectra almost unchanged after low-temperature thermal treatment, indicating that the formation of V_{CN} will not affect the crystal phase and composition of NiFe PBAs.

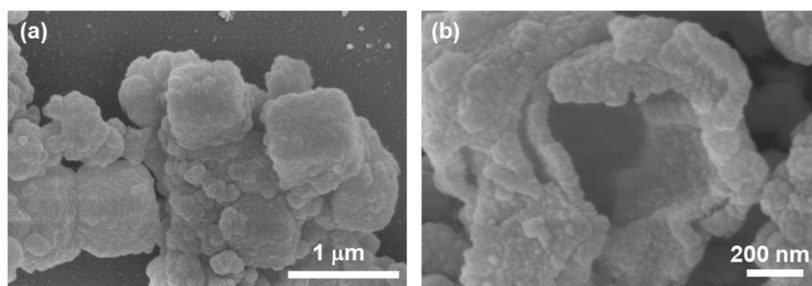


Fig. S8. (a) Low- and (b) high- magnification SEM images of PBAs-NG/C.

Fig. S8 shows that the calcined double-shelled NiFe PBA nanocage with a rough surface and still retains the original structure.

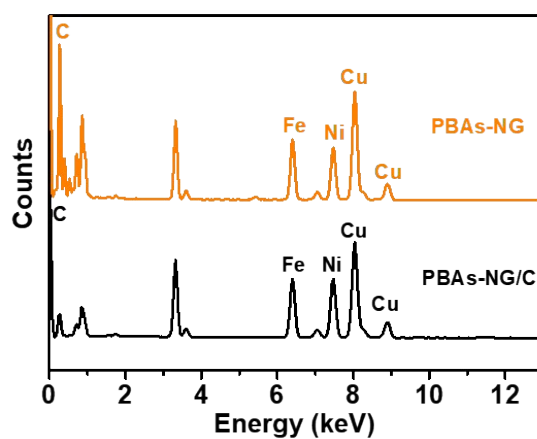


Fig. S9. The corresponding EDS spectra of PBAs-NG and PBAs-NG/C.

EDS spectra (Fig. S9) show the coexistence of K, Ni, Fe, C, and N both in the PBAs-NG and PBAs-NG/C. The Fe/Ni atomic ratios obtained from EDS testing for the two samples are close to the stoichiometric ratio of 1:1.

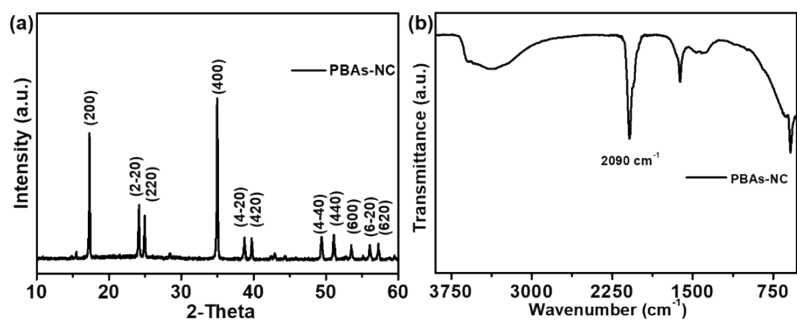


Fig. S10. (a) XRD pattern and (b) FT-IR spectrum of PBAs-NC.

The diffraction peaks of NiFe PBAs nanocubes in Fig. S10a agree well with previous NiFe PBAs structures.⁴ The band centered at 2090 cm⁻¹ is assigned to the CN group coordinated by Ni²⁺ and Fe²⁺ stretch (Fig. S10b), as demonstrated by previous works.⁵

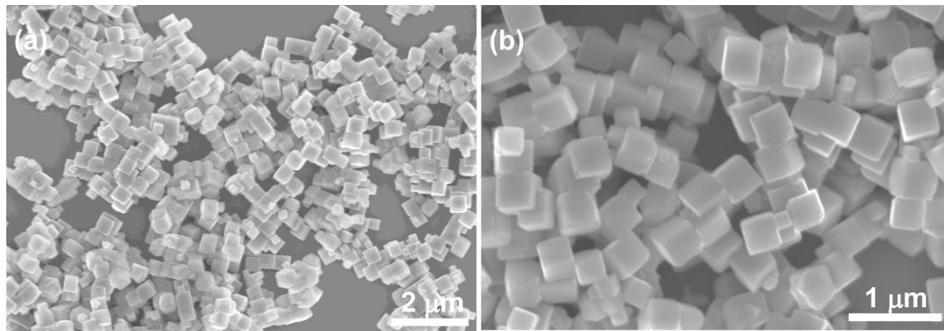


Fig. S11. (a) Low- and (b) high- magnification SEM images of NiFe PBAs nanocubes.

The SEM image shows that the NiFe PBAs have cubic morphology with an average side length of about 500 nm.

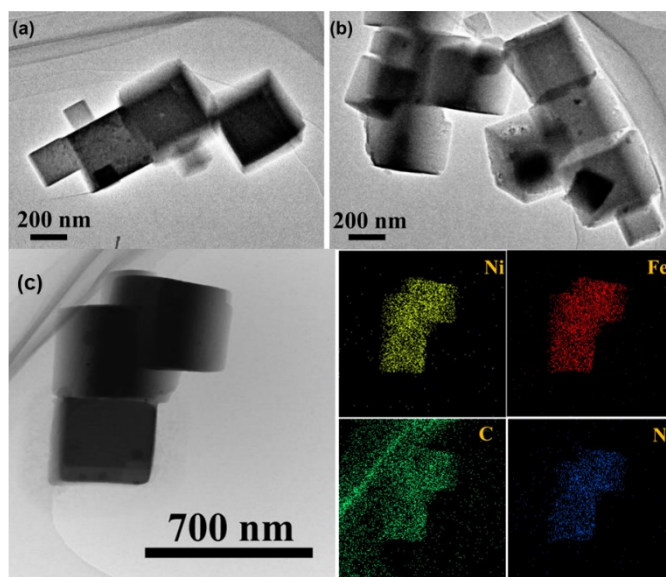


Fig. S12. (a, b) TEM images of solid NiFe PBAs nanocubes. (c) TEM image and corresponding EDS mapping of NiFe PBAs nanocubes.

The NiFe PBAs nanocubes show homogeneous distribution of Fe, Ni, C, N elements throughout the solid cube structures.

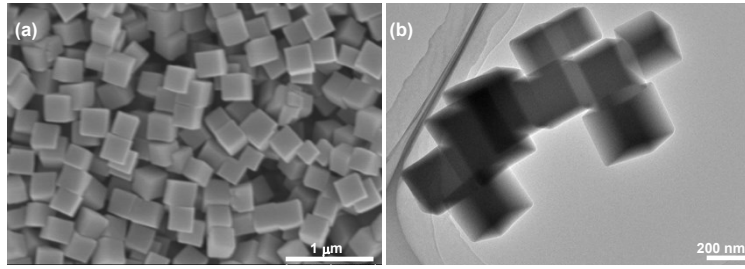


Fig. S13. (a) SEM image and (b) TEM image of PBA-NC/C.

After calcination, the as-prepared PBAs-NC/C still keeps the similar cubic morphology.

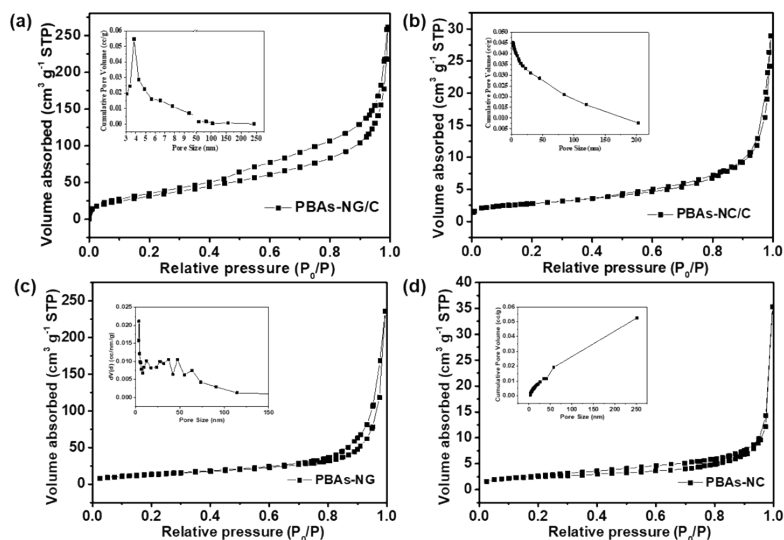


Fig. S14. N_2 adsorption-desorption isotherms of (a) PBAs-NG/C, (b) PBAs-NC/C, (c) PBAs-NG and (d) PBAs-NC electrocatalysts.

N_2 adsorption-desorption measurements show that the double-shelled PBAs-NG/C nanocages possess much higher specific surface area of $130.73 \text{ m}^2 \text{ g}^{-1}$ and total pore volume of $0.396 \text{ cm}^3 \text{ g}^{-1}$ than the PBAs-NG ($98.65 \text{ m}^2 \text{ g}^{-1}$, $0.273 \text{ cm}^3 \text{ g}^{-1}$), PBAs-NC/C ($9.82 \text{ m}^2 \text{ g}^{-1}$, $0.045 \text{ cm}^3 \text{ g}^{-1}$) and PBAs-NC ($6.12 \text{ m}^2 \text{ g}^{-1}$, $0.053 \text{ cm}^3 \text{ g}^{-1}$).

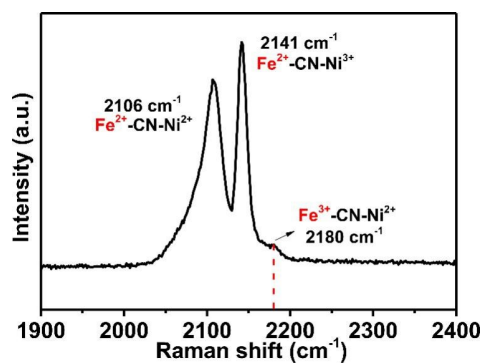


Fig. S15. Raman spectrum of PBAs-NC after calcination for 4 hours in N₂ atmosphere (PBAs-NC/C).

Raman spectrum reveals that PBAs-NC/C still retains the vibration peak belonging to CN groups at 2180 cm⁻¹ in the form of Fe³⁺-CN-Ni²⁺, indicating that the doubled-shelled NiFe PBAs nanocages are easier to overcome the energy barrier and form CN defects than the solid NiFe PBA nanocubes.

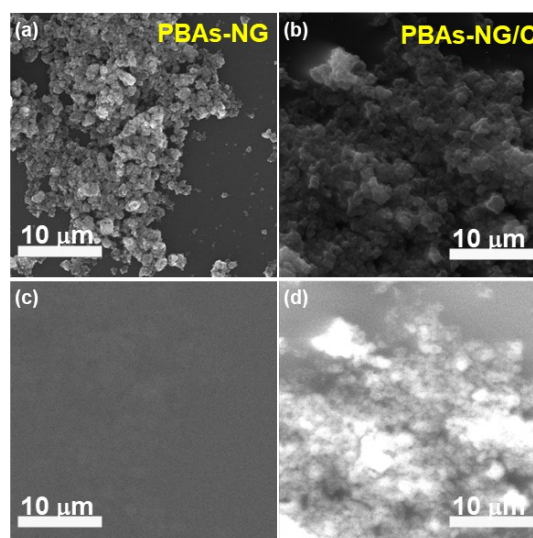


Fig. S16. (a) SEM image and (c) CL image of PBAs-NG. (b) SEM image and (d) CL image of PBAs-NG/C.

Considering that CN defects are able to tune the cathodoluminescence (CL) properties, the CL measurements were conducted on PBAs-NG and PBAs-NG/C for comparison. It is clear that PBAs-NG/C has the stronger CL signals than PBAs-NG, probably due to the high quantum efficiency of excitons localized at the CN vacancies sites.

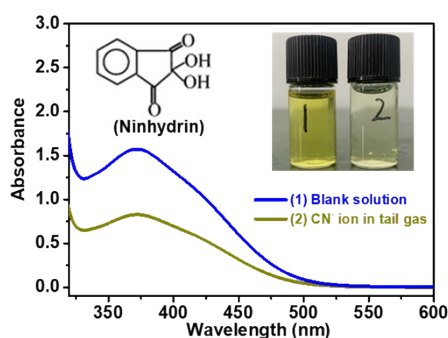


Fig. S17. Detection of cyanide in the tail gas absorbed solution by a spectrophotometer.

Ninhydrin could be used as the color indicator to detect cyanide.⁶ Ninhydrin reacts with Na_2CO_3 to form the yellow product, which could be disassembled by cyanide to weaken the yellow color. The detection experiment of cyanide in tail gas is described as follows. A mixture aqueous solution composed of 0.4 wt.% ninhydrin and 2 wt.% Na_2CO_3 was prepared to detect cyanide in the tail gas. We then bubbled the mixed solution with tail gas produced during the thermal treatment of the NiFe PBAs. The mixed solution was stirred continuously for 30 min and the absorbance was measured by a spectrophotometer. The blank solution (sample 1 in inset) was first prepared by adding ninhydrin solution to Na_2CO_3 solution without bubbling with tail gas, which has a yellow color and shows a broad peak at a wavelength of 370 nm in the spectrum. By contrast, sample 2 (the mixed solution bubbled with the tail gas) shows obviously lighter color and weaker peak intensity at 370 nm, which proves the existence of a certain amount of CN^- ions in the tail gas absorbed solution.

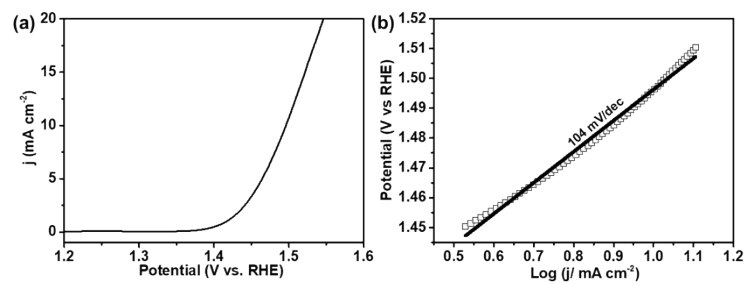


Fig. S18. (a) OER polarization curve of RuO₂ catalysts with iR-correction. Catalyst loading: ~ 0.15 mg cm⁻². Sweep rate: 5 mV s⁻¹. (b) Tafel plot of RuO₂ catalysts derived from polarization curve.

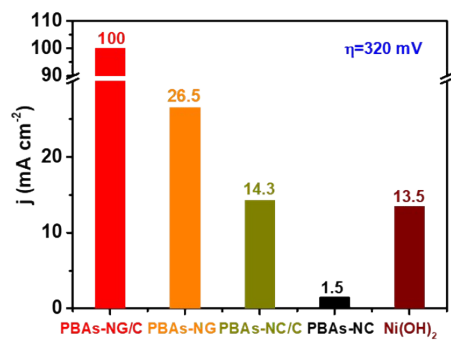


Fig. S19. The current density of different catalyst at the overpotential of 320 mV.

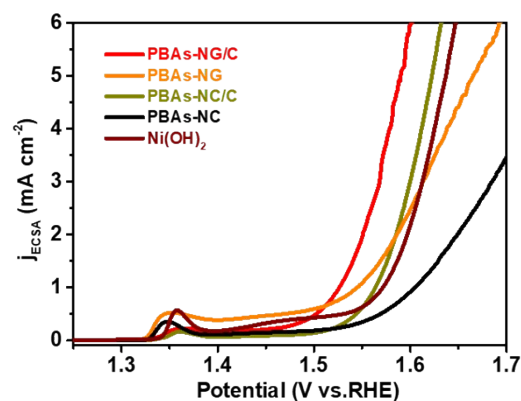


Fig. S20. OER polarization curves of different studied catalysts based on ECSA value.

We compare the specific activity of all samples by using electrochemically active surface area (ECSA) to calculate the current density ($j_{\text{ECSA}} = j/\text{ECSA}$). The ECSA values of all samples are estimated using an electrochemical capacitance measurement method.^{7,8} The intrinsic catalytic activity was investigated by the ECSA normalized linear sweep voltammetry (LSV) curves. The PBAs-NG/C catalyst needs only 296 mV overpotential to reach $1 \text{ mA cm}_{\text{ECSA}}^{-2}$, less than PBAs-NG (314 mV), PBAs-NC/C (334 mV), PBAs-NC (371 mV) and Ni(OH)₂ (343 mV).

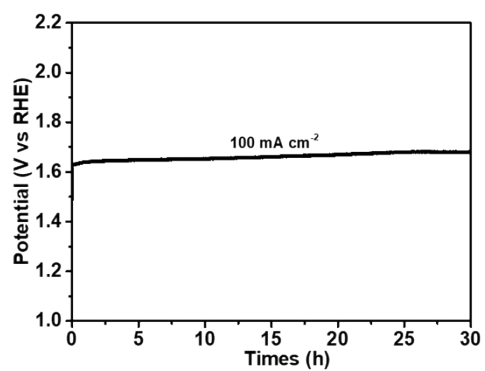


Fig. S21. Chronopotentiometric responses recorded on PBAs-NG/C at a constant current density of 100 mA cm^{-2} .

The PBAs-NG/C exhibits outstanding stability under higher current densities (100 mA cm^{-2}) for 30 h, revealing the superiority of PBAs-NG/C as promising stable OER electrocatalyst.

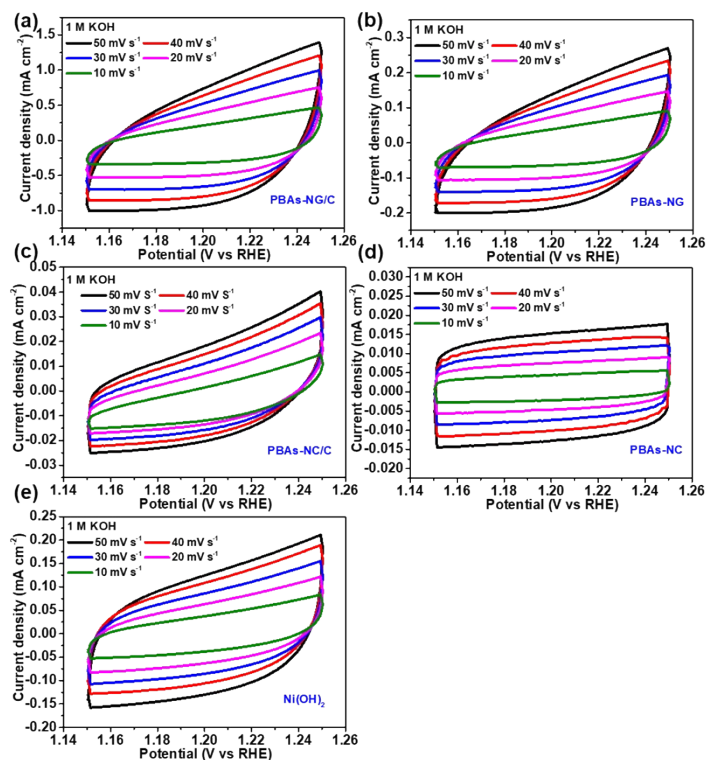


Fig. S22. Cyclic voltammogram curves of (a) PBAs-NG/C, (b) PBAs-NG, (c) PBAs-NC/C, (d) PBAs-NC and (e) Ni(OH)₂ modified electrodes in the double layer region at scan rates of 10, 20, 30, 40 and 50 mV s⁻¹ in 1.0 M KOH.

For the specific double-layer capacitor (C_{dl}) data, cyclic voltammetry (CV) curves were recorded in the non-Faradic region with scanning rate of 10, 20, 30, 40 and 50 mV s⁻¹, and the C_{dl} (mF cm⁻²) can be obtained by plotting the current difference (Δj) against the scanning rate.

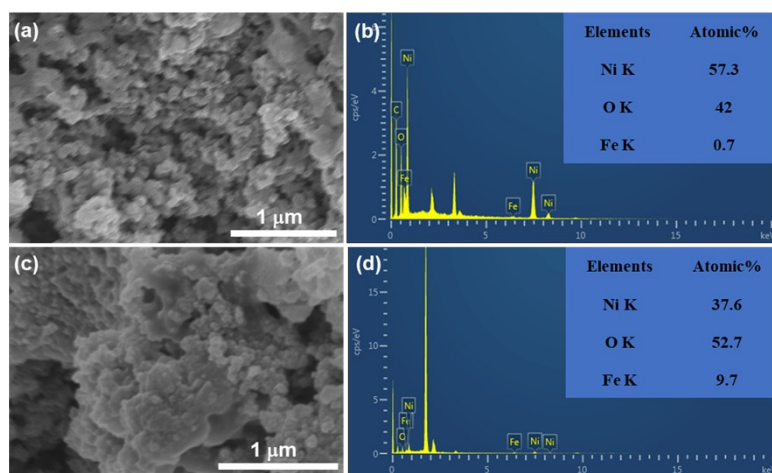


Fig. S23. SEM images and corresponding EDS spectra of the catalysts after OER measurement: (a, b) PBAs-NG, and (c, d) PBAs-NG/C.

Fig. S23a, 23c show the morphology of the PBAs-NG and PBAs-NG/C after CP test (50 hours) for OER, respectively. Compared with the original morphology, the morphology of nanocage is slightly in chaos after OER, with mixing with the carbon black. The EDS spectra simultaneously verify the existence of Ni, O and Fe elements in the PBAs-NG and PBAs-NG/C. However, the PBAs-NG/C has a higher atomic ratio of Fe element (9.7%) than PBAs-NG (0.7%), which may be relative to that the CN defect sites could suppress the Fe leaching in OER kinetic.

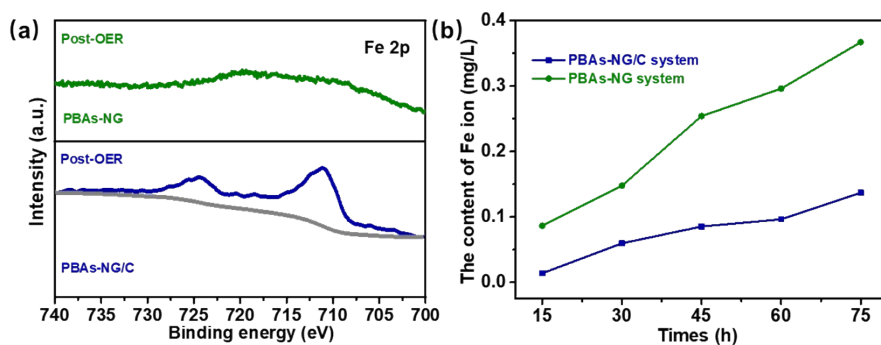


Fig. S24. (a) The Fe 2p XPS spectra of PBAs-NG and PBAs-NG/C after OER measurement, (b) ICP-MS results of Fe ions in the electrolyte during the chronopotentiometric measurement for the PBAs-NG/C and PBAs-NG electrocatalysts.

As widely known, the composition of NiFe PBA in alkaline electrolyte will gradually change with Fe element leaching into the electrolyte. However, the CN defect sites in PBAs-NG/C could suppress the Fe leaching to improve electrochemical activity, which was proved in previous reports.⁹ The PBAs-NG/C with CN defects have typical Fe 2p peaks with stronger intensity compared with the PBAs-NG without CN defects after OER process (Fig. S24a). The ICP-MS instrument was also utilized to characterize the content of Fe ion in the electrolyte during the chronopotentiometric measurement for the PBAs-NG/C and PBAs-NG electrocatalysts. As shown in Fig. S24b, the content of Fe in 1.0 M KOH electrolyte in the PBAs-NG/C system was obviously lower than that in the PBAs-NG system as OER process proceeds, which further demonstrates that the existence of CN defects could effectively reduce the loss of Fe.

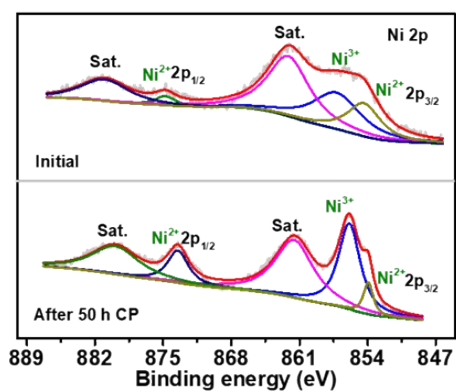


Fig. S25 The Ni 2p XPS spectra of PBAs-NG/C before and after OER measurement.

Fig. S25 shows the Ni 2p XPS spectra of PBAs-NG/C before and after chronopotentiometry test for 50 h at 20 mA cm^{-2} in 1.0 M KOH solution. The relative intensity of Ni³⁺ peak obviously increases after 50 h OER testing, suggesting Ni is readily oxidized to high valence as OER-active species.

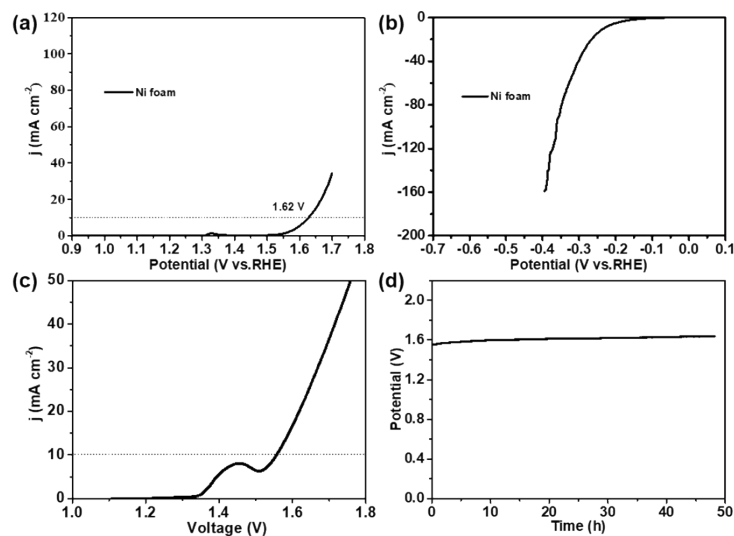


Fig. S26. (a) OER and (b) HER polarization curves for bare Ni foam. (c) Polarization curve of water electrolysis using PBAs-NG/C as OER and commercial Pt/C as HER catalysts in a 1.0 M KOH aqueous solution. (d) The durability test of the electrolytic cell at 10 mA cm^{-2} .

An electrolytic cell by using commercial Pt/C as a cathode and PBAs-NG/C as an anode, in which the catalyst powder was deposited on bare Ni foam, for overall water splitting was assembled to evaluate the properties of PBAs-NG/C as potential electrocatalyst in practical use. The bare Ni foam shows a negligible OER and HER activity. In contrast, the electrolytic cell exhibits a low overall voltage of 1.557 V for the heterogeneous overall water splitting at 10 mA cm^{-2} , demonstrating excellent performance at relatively low voltage. Moreover, the heterogeneous PBAs-NG/C based electrolytic cell can resist continuous electrolysis for 48 h at 10 mA cm^{-2} in a 1.0 M KOH aqueous solution at room temperature, indicating the excellent stability of PBAs-NG/C for overall water splitting.

Table S1 Synthetic methods of different defect(vacancy) in recent years.

NO.	Method	Defect(vacancy)	Chemical formula	Reference
1	Plasa treatment	C≡N	K ₂ NiFe(CN) ₆	9
2	Calcination	S	CuIn ₅ S ₈	10
3	Calcination	O	Ni-Mo/SiO ₂	11
4	Electrodeposition	S	(Fe-Ni)Co _x -OH/Ni ₃ S ₂	12
5	water-plasma	Co/Fe	CoFe LDH	13
6	Chemical etching	O	Co ₃ O ₄	14
7	Chemical etching	O	Fe _x Co _y Oxide	15

Table S2 The surface atomic ratio for PBAs-NG and derivatives obtained from XPS.

Sample	K/Ni	Fe/Ni	N/Ni	V_{CN} Content
PBAs-NG	1.58	1.08	5.78	0%
PBAs-NG/C-m	1.56	1.06	4.95	14.3%
PBAs-NG/C	1.57	1.03	4.71	18.5%

Table S3 The bulk atomic ratio for PBAs-NG and derivatives obtained from ICP-MS (measuring K, Fe, and Ni) and elemental analysis (measuring C and N).

Sample	K/Ni	Fe/Ni	N/Ni	C/N	C/Fe	V_{CN} Content
PBAs-NG	1.32	0.98	6.01	0.99	5.84	0%
PBAs-NG/C-m	1.26	0.95	5.25	1.01	5.36	12.6%
PBAs-NG/C	1.33	0.96	5.03	0.99	4.99	16.3%

Table S4 The bulk atomic ratio for PBAs-NC and derivatives obtained from ICP-MS (measuring K, Fe, and Ni) and elemental analysis (measuring C and N).

Sample	Na/Ni	Fe/Ni	N/Ni	C/N	C/Fe	V_{CN} Content
PBAs-NC	2.31	1.24	6.42	0.86	6.01	0%
PBAs-NC/C	2.20	1.19	6.20	0.86	5.86	3.43%

Table S5 The surface atomic ratio for PBAs-NC and derivatives obtained from XPS.

Sample	Na/Ni	Fe/Ni	N/Ni	V_{CN} Content
PBAs-NC	1.85	1.25	5.58	0%
PBAs-NC/C	1.89	1.28	5.34	4.3%

Table S6 Lists of activation energy and half-life of reaction for CN departure from different crystal surfaces.

	CN-010	CN-110-FeNi	CN-110- dangling	CN-bulk
activation energy (eV)	4.44	2.45	1.4	4.96
half-life of reaction (s)	6.23×10^{33}	5.63×10^{12}	44.5	1.96×10^{39}

Table S7 Comparison of onset potential and overpotential (η) at 10 and 20 mA cm⁻² for various OER catalysts.

Catalysts	Onset potential (mV)	J (mA cm ⁻²)	η (mV)	Electrolyte	Reference Electrode	Reference
Double-shelled NiFe PBAs with CN vacancy	172	20	267	1.0 M KOH	Hg/HgO	This work
NiFe PBAs With CN vacancy	225	10	280	1.0 M KOH	Hg/HgO	9
CoO _x with O vacancy	240	10	306	1.0 M KOH	Ag/Agcl	16
Co _{1-x} S/rGO with Co vacancy	260	10	310	1.0 M KOH	Ag/Agcl	17
CoFe-LDH with Co, Fe, O vacancy	~255	10	290	1.0 M KOH	Ag/Agcl	18
Co-Fe PBAs@PAN	~230	10	456	1.0 M KOH	Hg/HgO	19
Co-Fe core-shell PBAs	~235	10	271	1.0 M KOH	Hg/HgO	20
Ni _{0.6} Co _{1.4} P	~285	10	300	1.0 M KOH	Hg/HgO	21
Ni-Fe-doped K _{0.23} MnO ₂	~250	10	270	1.0 M KOH	Hg/HgO	22
NiFe Oxide	~195	10	271	1.0 M KOH	Ag/Agcl	23
NiCo-S@CoFe PBAs	~205	10	268	1.0 M KOH	Ag/Agcl	24
O-CNT/NiFe PBAs	~260	10	279	1.0 M KOH	Ag/Agcl	25

Table S8 The EIS fitting data of different catalysts at ~1.3 V vs. Hg/HgO.

Samples	$R_s(\Omega)$	$R_{ct}(\Omega)$	CPE(F)
PBA _s -NG/C	1.251	3.923	0.9197
PBA _s -NG	2.056	10.26	0.7457
PBA _s -NC/C	3.06	5.893	0.8052
PBA _s -NC	2.232	18.46	0.8183
Ni(OH) ₂	2.446	47.58	0.6894

References

- 1 B. Giraldo, W. C. Yeh and N. P. Kobayashi, *J. Mater. Sci.*, 2020, **55**, 14105-14111.
- 2 M. M. M. Mohammed, A. G. Abd-Elrahim and D. M. Chun, *Mater. Chem. Phys.*, 2020, **244**, 122701.
- 3 Q. Ren, R. Wang, H. Wang, J. Key, D. J. L. Brett, S. Ji, S. Yin and S. P. Kang, *J. Mater. Chem. A*, 2016, **4**, 7591-7595.
- 4 X. Su, Y. Wang, J. Zhou, S. Gu, J. Li and S. Zhang, *J. Am. Chem. Soc.*, 2018, **140**, 11286-11292.
- 5 W. A. S. Kavita, M. Jeerage and D. T. Schwartz, *Langmuir*, 2002, **18**, 3620-3625.
- 6 P. Nagaraja, M. S. H. Kumar, H. S. Yathirajan and J. S. Prakash, *Anal. Sci.*, 2002, **18**, 1027-1030.
- 7 Y. Feng, X. Wang, J. Huang, P. Dong, J. Ji, J. Li, L. Cao, L. Feng, P. Jin and C. Wang. *Chem. Eng. J.*, 2020, **390**, 124525.
- 8 P. Liu, B. Chen, C. W. Liang, W. T. Yao, Y. Z. Cui, S. Y. Hu, P. C. Zou, H. Zhang, H. J. Fan and C. Yang, *Adv. Mater.*, 2021, **33**, 2007377.
- 9 Z. Y. Yu, Y. Duan, J. D. Liu, Y. Chen, X. K. Liu, W. Liu, T. Ma, Y. Li, X. S. Zheng, T. Yao, M. R. Gao, J. F. Zhu, B. J. Ye and S. H. Yu, *Nat. Commun.*, 2019, **10**, 2799.
- 10 X. D. Li, Y. F. Sun, J. Q. Xu, Y. J. Shao, J. Wu, X. L. Xu, Y. Pan, H. X. Ju, J. F. Zhu and Y. Xie, *Nat. Energy*, 2019, **4**, 690-699.
- 11 F. Yang, N. J. Libretto, M. R. Komarneni, W. Zhou, J. T. Miller, X. Zhu and D. E. Resasco, *ACS Catal.*, 2019, **9**, 7791-7800.

- 12 Q. Che, Q. Li, X. Chen, Y. Tan and X. Xu, *Appl. Catal., B*, 2020, **263**, 118338.
- 13 R. Liu, Y. Y. Wang, D. D. Liu, Y. Q. Zou and S. Y. Wang, *Adv. Mater.*, 2017, **29**, 1701546.
- 14 Y. Wang, T. Zhou, K. Jiang, P. Da, Z. Peng, J. Tang, B. Kong, W.-B. Cai, Z. Yang and G. Zheng, *Adv. Energy Mater.*, 2014, **4**, 1400696.
- 15 L. Zhuang, L. Ge, Y. Yang, M. Li, Y. Jia, X. Yao and Z. Zhu, *Adv. Mater.*, 2017, **29**, 1606793.
- 16 W. Xu, F. Lyu, Y. Bai, A. Gao, J. Feng, Z. Cai and Y. Yin, *Nano Energy*, 2018, **43**, 110-116.
- 17 J. Zhu, Z. Ren, S. Du, Y. Xie, J. Wu, H. Meng, Y. Xue and H. Fu, *Nano Res.*, 2017, **10**, 1819-1831.
- 18 R. Liu, Y. Wang, D. Liu, Y. Zou and S. Wang, *Adv. Mater.*, 2017, **29**, 1701546.
- 19 L. J. Yang, S. Z. Feng, G. C. Xu, B. Wei and L. Zhang, *ACS Sustainable Chem. Eng.*, 2019, **7**, 5462-5475.
- 20 W. Zhang, H. Song, Y. Cheng, C. Liu, C. Wang, M. A. N. Khan, H. Zhang, J. Liu, C. Yu, L. Wang and J. Li, *Adv. Sci.*, 2019, **6**, 1801901.
- 21 B. Qiu, L. Cai, Y. Wang, Z. Lin, Y. Zuo, M. Wang and Y. Chai, *Adv. Funct. Mater.*, 2018, **28**, 1706008.
- 22 H. Liao, X. Guo, Y. Hou, H. Liang, Z. Zhou and H. Yang, *Small*, 2020, **16**, 1905223.
- 23 A. Kumar and S. Bhattacharyya, *ACS Appl. Mater. Interfaces*, 2017, **9**, 41906-41915.
- 24 M. H. Kahnamouei and S. Shahrokhian, *ACS Appl. Mater. Interfaces*, 2020, **12**, 16250-16263.
- 25 Y. C. Lin, C. H. Chuang, L. Y. Hsiao, M. H. Yeh and K. C. Ho, *ACS Appl. Mater. Interfaces*, 2020, **12**, 42634-42643.